PROCEEDINGS OF SCIENCE

Measurement of iron cosmic-ray primaries below 10GeV/n by use of the geomagnetic effect with CALET

M.Ichimura[a,*] **and K.Kasahara**[b] **for the CALET collaboration**

[a] *Faculty of Science and Technology, Graduate School of Science and Technology, Hirosaki University, 3, Bunkyo, Hirosaki, Aomori 036-8561, Japan*

[b] *Department of Electronic Information Systems, Shibaura Institute of Technology, 307 Fukasaku, Minuma, Saitama 337-8570, Japan*

E-mail: ichimu@hirosaki-u.ac.jp

The CALET Calorimeter on the International Space Station(ISS) has previously measured the flux and spectrum of iron cosmic-ray nuclei above 10 GeV/n. In order to extend the measurement to the region below 10 GeV/n, we carry out an analysis to utilize the geomagnetic effect. Cutoff rigidities of cosmic-ray nuclei are calculated for all directions for each observation point in the ISS orbit. The integral spectrum of observed rigidities is then obtained by counting the number of iron nuclei in each bin of cutoff rigidity. The absolute flux and differential spectrum are then calculated by taking the detection efficiencies into account. Here we present the details of the analysis procedure and the iron spectrum below 10 GeV/n.

38th International Cosmic Ray Conference (ICRC2023)
26 July - 3 August, 2023
Nagoya, Japan

*Speaker

PoS(ICRC2023)057

1. Introduction

The CALET experiment has achieved the measurement of the flux and the energy spectra of various kinds of cosmic-ray nuclei to reveal the origin, acceleration, and propagation mechanisms[1–5]. The energy spectrum for the iron primaries has been published by CALET for the energy region from 10 GeV/n to more than 1 TeV/n[6]. We performed flux calculations using the geomagnetic cutoff to obtain the iron spectrum to a lower energy region, less than 10 GeV/n. The details of the analysis procedure and the result will be reported here.

2. CALET instrument

The CALET calorimeter consists of three parts. The upper part, the CHarge Detector (CHD), is composed of two layers of 1 cm thick plastic scintillators, CHDx and CHDy. It is used for the charge determination of the incident particles. Below that, the Imaging Calorimeter (IMC) is installed. It consists of 448 scintillating fibers with a cross-section of 1 mm by 1 mm, stacked one layer each in the orthogonal x and y directions, alternating with tungsten plates. It is used for the track reconstruction and the detailed study of the shower development. The lower part is the Total AbSorption Calorimeter (TASC), which is composed of twelve layers of 2 cm thick PWO scintillators stacked in the x and y directions. It is used for energy determination. Details on the instrument can be found in the Supplemental Material (SM) of Ref. [7]. In this study, only the CHD and IMC were used for the analysis.

3. Data analysis

3.1 Calculation of cutoff rigidity by the backtracing method

First, cutoff rigidity calculations were performed for every direction at observation points along the ISS orbit. The geomagnetic field at a fixed time is calculated by the geomagnetic field models, IGRF13(International Geomagnetic Reference Field)[8] and TS05[9]. IGRF is a standard model for the internal magnetic field. TS05 is a model for the external magnetic field with the disturbance caused by solar wind. The calculation of the geomagnetic field is performed by these two models together. Note that TS05 uses solar wind parameters based on actual measurements, and the data in the periods without solar wind observation data are not used in this analysis.

Next, the latitude, longitude, and altitude of the observation point are set, and an antiproton is emitted in the direction of a certain zenith angle and a certain azimuthal angle with a certain rigidity R. Then, while solving the motion equations using the Runge-Kutta method, the particle track is traced. The tracing process is stopped when;

(1) the particle hit the Earth

(2) the particle reached the magnetopause

(3) the particle is far from the Earth more than 15 times the Earth's radius.

In case (1), this condition is classified in the forbidden region. A nucleus cannot enter from this direction with this rigidity. In cases (2) and (3), these conditions are classified in the allowed region.

A nucleus can enter from this direction with this rigidity. We repeat this backtracing process while varying the value of Rigidity, and determine whether the trajectory fell into the forbidden region or the allowed region. Rigidity is varied with the step of 0.01 in logarithmic scale from 1 GV to 50 GV. In the results of this calculation, we can observe the alternating appearance of the forbidden region and allowed region which is known as the penumbra region. We process this penumbra region according to the method described in Ref. [10], and calculate the effective cutoff rigidity, which is then adopted as the final cutoff rigidity. For simplicity, we use the parameter $\beta = -1$ in the calculations described in Ref. [10].

At each observation point, the above calculation is performed for all zenith angles and azimuthal angles, and the cutoff rigidity dome (Rc dome) is calculated as shown in Fig. 1. The hemisphere is divided into 193 bins, and the cutoff rigidity Rc is calculated for each direction. In the azimuthal direction, it is divided into 24 bins at 15-degree intervals. In the zenith angle direction, it is divided into 6 parts with equal steps in the scale of $\cos\theta d(\cos\theta)$. The colors in the figure represent the values of Rc. This calculation was performed for 30 degrees north latitude and 135 degrees east longitude. The east-west effect is clearly visible. In this analysis, the region within a zenith angle of 45 degrees was used.

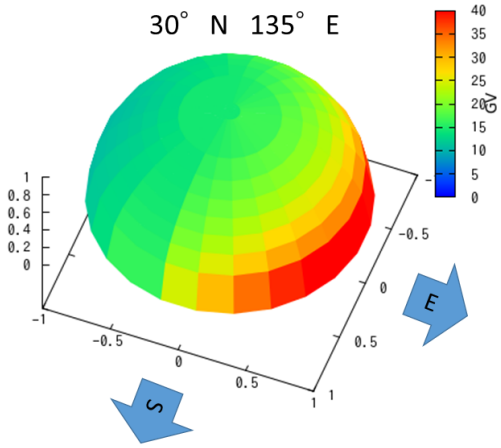

Figure 1: Rc dome at LAT 30N LON 135E. Cutoff rigidity values on the east side are higher than on the west side. The cutoff rigidity depends on the incident direction.

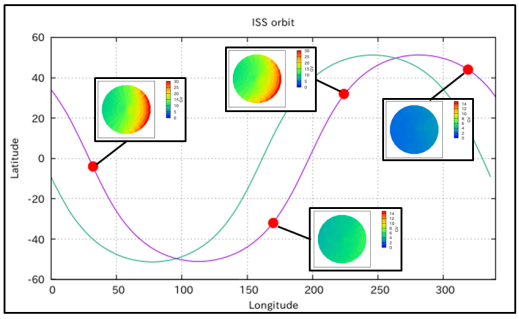

Figure 2: Rc domes are calculated along the ISS orbit. The cutoff rigidity depends on latitude, longitude, and altitude. The latitude dependence is the strongest. At higher latitudes, the cutoff rigidity is generally smaller in all directions.

The calculation of such Rc domes was performed for each observation point along the ISS orbit as shown Fig. 2. The analysis period is 68 months from October 2015 to May 2021, and the UH trigger mode[11] periods have been picked up.

First, the longitude and latitude of observation points continuously recorded along the ISS orbit were digitized at 1 degree intervals. These points were further grouped into sets of 10 points, and a representative point was determined for each set. The calculations of the Rc dome were performed for these representative points. The total number of observation points considered in the calculation was about 25,000 points per month. The obtained Rc values were used in the subsequent analysis. Note that the analysis has been done for the periods with solar wind observation data only because

the geomagnetic field calculation needs actual solar wind data.

3.2 Observation data analysis

The analysis of flight data involved selecting data triggered by the UH trigger from the observation data collected over a period of 68 months, from October 2015 to May 2021. The UH trigger mode requires signals above a certain threshold at the CHD and the top four layers of the IMC.

3.2.1 Charge determination

A cross-plot of the CHDx and CHDy signals with zenith angle correction was made for the picked-up tracks as shown in Fig. 3(a). The main cosmic ray nuclei from oxygen to iron are clearly seen. Tracks with a difference between CHDx and CHDy within 10% were selected (Fig. 3(b)), and histograms were generated for CHDx and CHDy respectively. Fig. 3(c) shows the histogram for CHDx. By reading the peak values for each nucleus component from this histogram, representative values for each nucleus can be obtained.

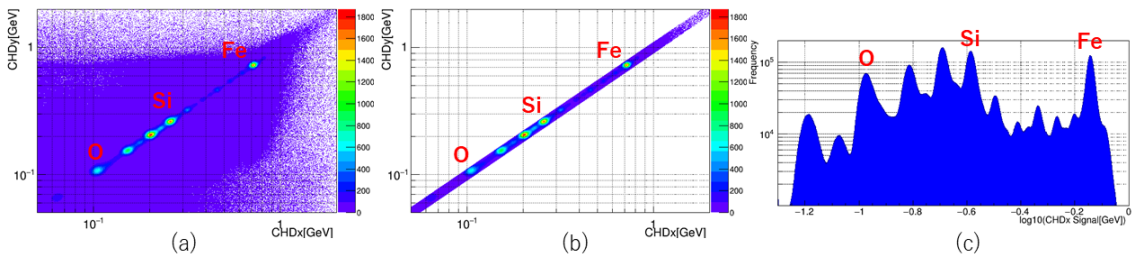

Figure 3: For the all tracks triggered by the UH trigger; (a) the CHDy signal vs the CHDx signal. There are some clusters corresponds to the major component of cosmic ray nuclei. (b) The tracks with CHDx and CHDy signals within 10% of each other. (c) The histogram of CHDx signal for the tracks in the plot (b). The horizontal axis shows $\log_{10}$(CHDx).

The representative value of the CHD signal is expected to depend on rigidity. Therefore, we divided the Rc range from $10^{0.50}$ GV to $10^{1.30}$ GV into 16 equal parts on a log scale and performed charge determination for each bin. Additionally, tracks with rigidity greater than $10^{1.30}$ GV(19.95 GV) were grouped together as the 17th bin, and charge determination was done similarly. For each Rc bin, the representative values of CHDx and CHDy corresponding to each nucleus component were obtained. Then, for the conversion to charge, the relationship between the CHD signal and the atomic number squared (z^2) was fitted using the halo model [12], which considers the quenching effect in a scintillator. Fig. 4 shows examples of plots of CHDx vs z^2 for several Rc bins and the fitted curves. Using this curve, estimated charges (Zx, Zy) corresponding to CHDx and CHDy were calculated for each Rc bin.

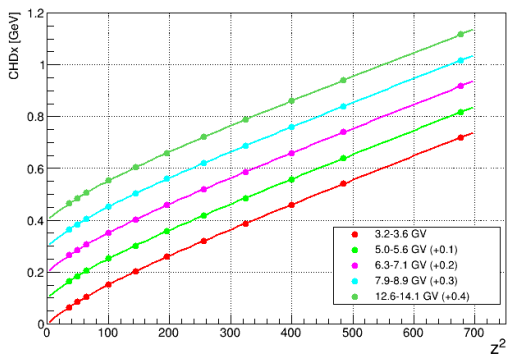

Figure 4: CHDx signal vs z^2 with fitting curves by the halo mode[12] for the 5 different Rc bins. This fitting has been done for each of the 17 Rc bins.

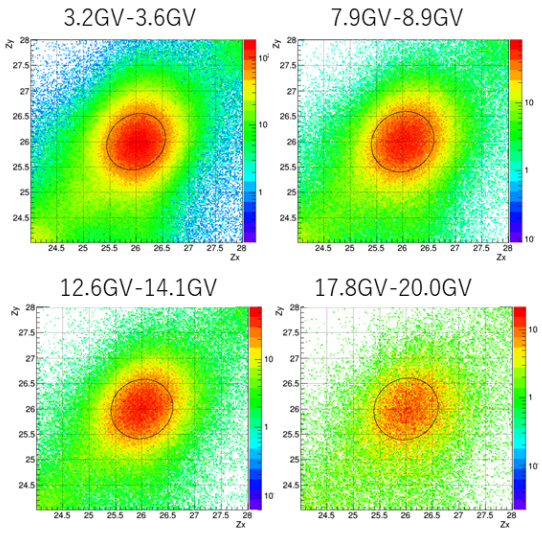

Figure 5: Zy vs Zx plots for several Rc bins. Ellipses for 1.2σ are demonstrated. The tracks in the 1.2σ ellipse have been selected as candidates for iron nuclei.

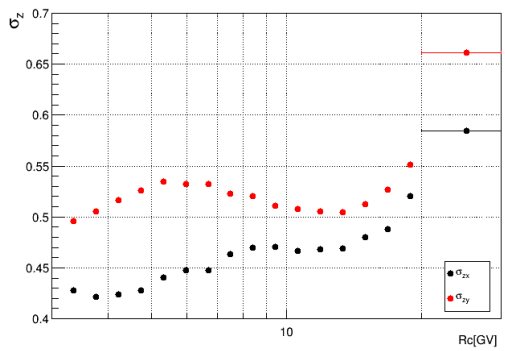

Figure 6: The standard deviation for the estimated charges by CHDx and CHDy. The horizontal axis shows Rc values. Points correspond to each of the 17 Rc bins. σ_{zy} is greater than σ_{zx}. The last bin represents the Rc range greater than 19.95 GV.

3.2.2 Calculation of the flux

Figure 5 shows a 2D histogram of Zy vs Zx for four Rc bins. One can see that the distribution is centered around Z = 26.0. The resolution (1 σ) of the estimated charges from CHDx and CHDy is shown in Fig. 6. They are in the range of 0.40-0.55 charge units except for the highest bin which is for the tracks with Rc greater than 19.95 GV. The ellipse drawn in Fig. 5 represents the 1.2 σ line. Iron candidates were selected inside an ellipse with minor and major semi-axes 1.2 σ_{zx} and 1.2 σ_{zy}, respectively, rotated clockwise by 45 degrees.

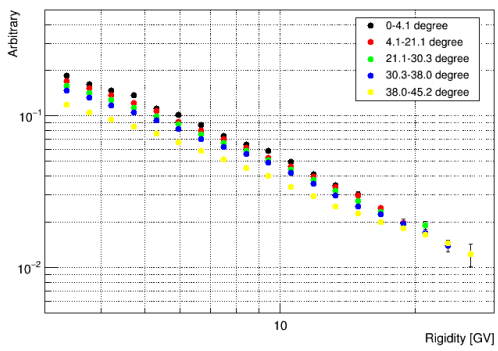

Figure 7: The integral rigidity spectrum of iron nuclei. It is obtained by counting the number of iron nuclei for each Rc bin and dividing by solid angle × observation time. The colors represent different ranges of zenith angles.

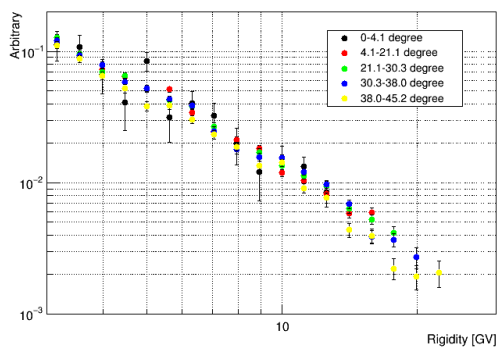

Figure 8: The Differential rigidity spectrum of iron nuclei converted from Fig. 7.

For the adopted iron nucleus candidates, since the arrival time and direction are known, they can be associated with Rc for each observation point and incident direction that was calculated beforehand. By counting the number of iron nuclei in each Rc bin and simultaneously using the number of solid angle bins and the sum of live time for the corresponding Rc bin, an integrated rigidity spectrum was calculated. The results are shown in Fig. 7. The different colors represent different ranges of zenith angles. This spectrum was converted to a differential spectrum as shown in Fig. 8.

3.2.3 Detection efficiency

For the absolute flux, geometric and tracking efficiencies were calculated. The Cosmos + Epics simulation code[15, 16] was used for this calculation. Iron nuclei were incident on the CALET detector, and the detection efficiency was calculated using the same UH trigger and track reconstruction algorithms as the observed data. The results are shown in Fig. 9. The horizontal axis represents the kinetic energy per particle, and the colors represent different ranges of zenith angles. For the nuclear interaction model, the PHITS model[13] is used for kinetic energies below 2 GeV/n(112 GeV/particle), and the JAM model[14] is used for kinetic energies between 2 GeV/n and 100 GeV/n(112 GeV/particle and 5.6 TeV/particle).

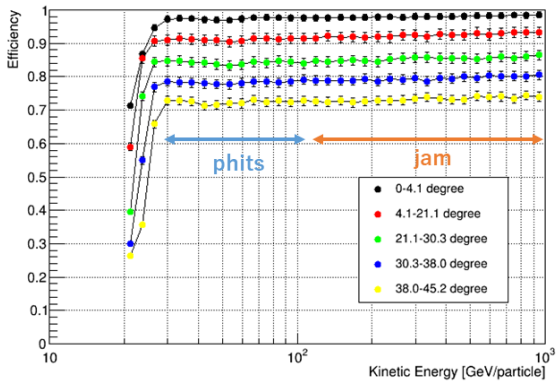

Figure 9: Tracking and Geometrical efficiency of iron nuclei. It is calculated by the simulation code Cosmos8.042 + Epics9.311. Two different interaction models, the phits and the jam, are used for this calculation. The color shows different zenith angle ranges. Larger zenith angles have more interaction, so the efficiency becomes lower.

From the plot, one can see that the efficiency decreases with increasing zenith angle due to the effects of nuclear interactions. Additionally, the steep drop below 30 GeV is due to particles stopping in the upper 4 layers of the IMC due to ionization losses. The geometric and tracking efficiency for vertical incident particles is about 98%. These detection efficiencies were applied to the previous differential spectrum to calculate the absolute flux.

3.2.4 Systematic uncertainties

The systematic uncertainties were evaluated as follows. First, the fluctuation of flux due to the precision of cutoff rigidity determination was studied. The influence of bin width in longitude and latitude on the flux was about 8%. Additionally, the effect of the variation of Rc within the solid angle bin was about 5%. Next, the effect of the charge identification cut was examined. In the analysis, the charge identification cut was done at 1.2 σ. The flux variation was investigated by applying cuts at 1.1 σ and 1.3 σ, resulting in a variation of less than 2%. Furthermore, for the checking of longterm stability, the data were divided into yearly segments, and the flux was calculated for each year. The estimated variation was up to about 10%. At this stage, the systematic uncertainty due to the interaction model is not considered yet.

3.2.5 Absolute flux

Figure 10 shows the rigidity spectrum of the iron nuclei obtained by this work. The vertical axis represents the differential absolute flux. The error bars show the statistical errors and the colored band indicates the quadrature sum of statistical and systematic errors. The systematic errors include the sources described in the section 3.2.4. Flux has been calculated from 3 GV to more than 20 GV. It seems that the rigidity spectrum follows a single power law with a power index about -2.0.

The energy spectrum with kinetic energy per nucleon from 1 GeV/n to 10 GeV/n is shown in Fig. 11. The vertical axis represents the flux multiplied by $E^{2.6}$. The meaning of the error bars and the colored band is the same as Fig. 10.

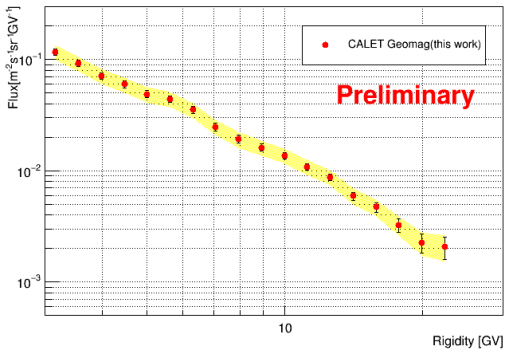

Figure 10: The rigidity spectrum of the absolute flux for iron nuclei obtained by this work(red points). The detection efficiencies are taken into account for each zenith angle range, then combined in one spectrum. The error bars show the statistical errors and the colored band indicates the quadrature sum of statistical and systematic errors.

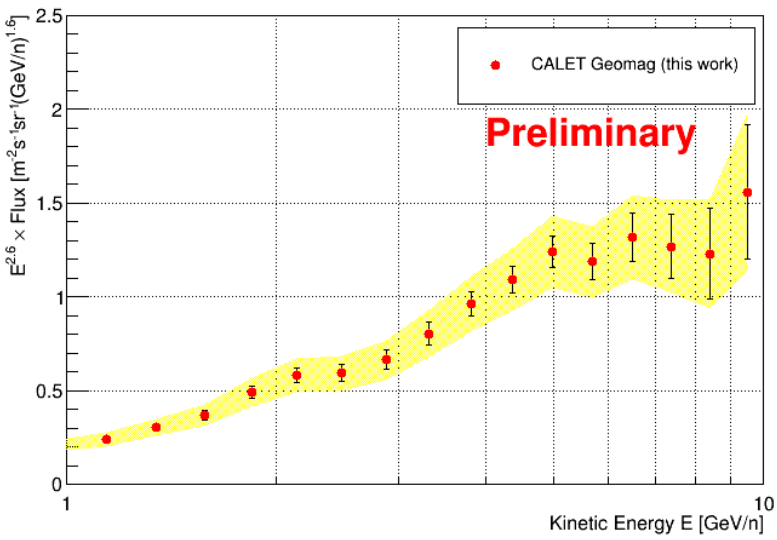

Figure 11: The energy spectrum of the absolute flux for iron nuclei. The horizontal axis shows the kinetic energy per nucleon. The red points are the results obtained by this work. The error bars show the statistical errors and the yellow zone indicates the quadrature sum of statistical and systematic errors.

In this analysis, only the events with a zenith angle within 45 degrees were analyzed using a limited period of the observations until May, 2021. However, by including tracks with larger zenith angles in the analysis, it is possible to increase the statistics up to larger values of Rc and extend the spectrum towards higher rigidities.

In this energy range, the flux undergoes significant variations due to solar modulation. In order to compare our results with other observations, it is necessary to quantitatively evaluate the solar modulation effect for each observation period. This will be a future work.

4. Conclusion

From the CALET observation data, we obtained the rigidity spectrum of the absolute flux for iron nuclei in the range of 3 GV to more than 20 GV, which follows a single power law with a power index about -2.0 by use of the geomagnetic effect. It has been converted to the energy spectrum of the absolute flux in the energy region about 1 GeV/n to 10 GeV/n. We will increase the data in the 7 GeV/n to 10 GeV/n range, and will extend the spectrum until it overlaps with the calorimeter results in the future. Furthermore, in order to compare our results with those of other groups, we will evaluate the effect of solar modulation for each observation period.

Acknowledgements

We gratefully acknowledge JAXA's contributions to the development of CALET and to the operations onboard the International Space Station. The CALET effort in Italy is supported by ASI under Agreement No. 2013- 018-R.0 and its amendments. The CALET effort in the United States is supported by NASA through Grants No. 80NSSC20K0397, No. 80NSSC20K0399, and No. NNH18ZDA001N-APRA18-0004. This work is supported in part by JSPS Grant-in-Aid for Scientific Research (S) Grant No. 19H05608 and (C) Grant No. 20K03982 in Japan.

References

[1] O. Adriani et al.(CALET Collaboration), *Phys.Rev.Lett.*, 129,101102(2022).

[2] O. Adriani et al.(CALET Collaboration), *Phys.Rev.Lett.*, 130,171002(2023).

[3] O. Adriani et al.(CALET Collaboration), *Phys.Rev.Lett.*, 129,251103(2022).

[4] O. Adriani et al.(CALET Collaboration), *Phys.Rev.Lett.*, 125,251102(2020).

[5] O. Adriani et al.(CALET Collaboration), *Phys.Rev.Lett.*, 128,131103(2022).

[6] O. Adriani et al.(CALET Collaboration), *Phys.Rev.Lett.*, 126,241101(2021).

[7] O. Adriani et al.(CALET Collaboration), *Phys.Rev.Lett.*, 119,181101(2017).

[8] P. Alken et al., *Earth Planets Space*, 73, 49(2021).

[9] N.A. Tsyganenko and M.I. Sitnov, *J. Geophys. Res.*, 110, A03208(2005).

[10] E. Kamioka et al., *Astroparticle Physics*, 6, 155(1997).

[11] A.W. Ficklin, N. Cannady, B.F. Rauch and W. Zober(CALET), *Pos(ICRC2021)*, 069(2021).

[12] P.S. Marrocchesi et al., *NIM*, A659, 477(2011).

[13] K. Niita et al., *Radiation Measurements*, 41, 1080(2006).

[14] Y. Nara et al., *Phys.Rev.C*, 61, 024901(1999).

[15] K. Kasahara, *Proc. of 24th Int. Cosmic Ray Conf.(Rome,Italy)*, 1, 399(1995).

[16] See EPICS webpage http://cosmos.n.kanagawa-u.ac.jp/EPICSHome/

Full Author List: CALET Collaboration

O. Adriani[1,2], Y. Akaike[3,4], K. Asano[5], Y. Asaoka[5], E. Berti[2,6], G. Bigongiari[7,8], W.R. Binns[9], M. Bongi[1,2], P. Brogi[7,8], A. Bruno[10], N. Cannady[11,12,13], G. Castellini[6], C. Checchia[7,8], M.L. Cherry[14], G. Collazuol[15,16], G.A. de Nolfo[10], K. Ebisawa[17], A.W. Ficklin[14], H. Fuke[17], S. Gonzi[1,2,6], T.G. Guzik[14], T. Hams[11], K. Hibino[18], M. Ichimura[19], K. Ioka[20], W. Ishizaki[5], M.H. Israel[9], K. Kasahara[21], J. Kataoka[22], R. Kataoka[23], Y. Katayose[24], C. Kato[25], N. Kawanaka[20], Y. Kawakubo[14], K. Kobayashi[3,4], K. Kohri[26], H.S. Krawczynski[9], J.F. Krizmanic[12], P. Maestro[7,8], P.S. Marrocchesi[7,8], A.M. Messineo[8,27], J.W. Mitchell[12], S. Miyake[28], A.A. Moiseev[29,12,13], M. Mori[30], N. Mori[2], H.M. Motz[18], K. Munakata[25], S. Nakahira[17], J. Nishimura[17], S. Okuno[18], J.F. Ormes[31], S. Ozawa[32], L. Pacini[2,6], P. Papini[2], B.F. Rauch[9], S.B. Ricciarini[2,6], K. Sakai[11,12,13], T. Sakamoto[33], M. Sasaki[29,12,13], Y. Shimizu[18], A. Shiomi[34], P. Spillantini[1], F. Stolzi[7,8], S. Sugita[33], A. Sulaj[7,8], M. Takita[5], T. Tamura[18], T. Terasawa[5], S. Torii[3], Y. Tsunesada[35,36], Y. Uchihori[37], E. Vannuccini[2], J.P. Wefel[14], K. Yamaoka[38], S. Yanagita[39], A. Yoshida[33], K. Yoshida[21], and W.V. Zober[9]

[1]Department of Physics, University of Florence, Via Sansone, 1 - 50019, Sesto Fiorentino, Italy, [2]INFN Sezione di Firenze, Via Sansone, 1 - 50019, Sesto Fiorentino, Italy, [3]Waseda Research Institute for Science and Engineering, Waseda University, 17 Kikuicho, Shinjuku, Tokyo 162-0044, Japan, [4]JEM Utilization Center, Human Spaceflight Technology Directorate, Japan Aerospace Exploration Agency, 2-1-1 Sengen, Tsukuba, Ibaraki 305-8505, Japan, [5]Institute for Cosmic Ray Research, The University of Tokyo, 5-1-5 Kashiwa-no-Ha, Kashiwa, Chiba 277-8582, Japan, [6]Institute of Applied Physics (IFAC), National Research Council (CNR), Via Madonna del Piano, 10, 50019, Sesto Fiorentino, Italy, [7]Department of Physical Sciences, Earth and Environment, University of Siena, via Roma 56, 53100 Siena, Italy, [8]INFN Sezione di Pisa, Polo Fibonacci, Largo B. Pontecorvo, 3 - 56127 Pisa, Italy, [9]Department of Physics and McDonnell Center for the Space Sciences, Washington University, One Brookings Drive, St. Louis, Missouri 63130-4899, USA, [10]Heliospheric Physics Laboratory, NASA/GSFC, Greenbelt, Maryland 20771, USA, [11]Center for Space Sciences and Technology, University of Maryland, Baltimore County, 1000 Hilltop Circle, Baltimore, Maryland 21250, USA, [12]Astroparticle Physics Laboratory, NASA/GSFC, Greenbelt, Maryland 20771, USA, [13]Center for Research and Exploration in Space Sciences and Technology, NASA/GSFC, Greenbelt, Maryland 20771, USA, [14]Department of Physics and Astronomy, Louisiana State University, 202 Nicholson Hall, Baton Rouge, Louisiana 70803, USA, [15]Department of Physics and Astronomy, University of Padova, Via Marzolo, 8, 35131 Padova, Italy, [16]INFN Sezione di Padova, Via Marzolo, 8, 35131 Padova, Italy, [17]Institute of Space and Astronautical Science, Japan Aerospace Exploration Agency, 3-1-1 Yoshinodai, Chuo, Sagamihara, Kanagawa 252-5210, Japan, [18]Kanagawa University, 3-27-1 Rokkakubashi, Kanagawa, Yokohama, Kanagawa 221-8686, Japan, [19]Faculty of Science and Technology, Graduate School of Science and Technology, Hirosaki University, 3, Bunkyo, Hirosaki, Aomori 036-8561, Japan, [20]Yukawa Institute for Theoretical Physics, Kyoto University, Kitashirakawa Oiwake-cho, Sakyo-ku, Kyoto, 606-8502, Japan, [21]Department of Electronic Information Systems, Shibaura Institute of Technology, 307 Fukasaku, Minuma, Saitama 337-8570, Japan, [22]School of Advanced Science and Engineering, Waseda University, 3-4-1 Okubo, Shinjuku, Tokyo 169-8555, Japan, [23]National Institute of Polar Research, 10-3, Midori-cho, Tachikawa, Tokyo 190-8518, Japan, [24]Faculty of Engineering, Division of Intelligent Systems Engineering, Yokohama National University, 79-5 Tokiwadai, Hodogaya, Yokohama 240-8501, Japan, [25]Faculty of Science, Shinshu University, 3-1-1 Asahi, Matsumoto, Nagano 390-8621, Japan, [26]Institute of Particle and Nuclear Studies, High Energy Accelerator Research Organization, 1-1 Oho, Tsukuba, Ibaraki, 305-0801, Japan, [27]University of Pisa, Polo Fibonacci, Largo B. Pontecorvo, 3 - 56127 Pisa, Italy, [28]Department of Electrical and Electronic Systems Engineering, National Institute of Technology (KOSEN), Ibaraki College, 866 Nakane, Hitachinaka, Ibaraki 312-8508, Japan, [29]Department of Astronomy, University of Maryland, College Park, Maryland 20742, USA, [30]Department of Physical Sciences, College of Science and Engineering, Ritsumeikan University, Shiga 525-8577, Japan, [31]Department of Physics and Astronomy, University of Denver, Physics Building, Room 211, 2112 East Wesley Avenue, Denver, Colorado 80208-6900, USA, [32]Quantum ICT Advanced Development Center, National Institute of Information and Communications Technology, 4-2-1 Nukui-Kitamachi, Koganei, Tokyo 184-8795, Japan, [33]College of Science and Engineering, Department of Physics and Mathematics, Aoyama Gakuin University, 5-10-1 Fuchinobe, Chuo, Sagamihara, Kanagawa 252-5258, Japan, [34]College of Industrial Technology, Nihon University, 1-2-1 Izumi, Narashino, Chiba 275-8575, Japan, [35]Graduate School of Science, Osaka Metropolitan University, Sugimoto, Sumiyoshi, Osaka 558-8585, Japan, [36]Nambu Yoichiro Institute for Theoretical and Experimental Physics, Osaka Metropolitan University, Sugimoto, Sumiyoshi, Osaka 558-8585, Japan, [37]National Institutes for Quantum and Radiation Science and Technology, 4-9-1 Anagawa, Inage, Chiba 263-8555, Japan, [38]Nagoya University, Furo, Chikusa, Nagoya 464-8601, Japan, [39]College of Science, Ibaraki University, 2-1-1 Bunkyo, Mito, Ibaraki 310-8512, Japan